Thermally Induced Structural Evolution and Performance of Mesoporous Block Copolymer-Directed Alumina Perovskite Solar Cells

Kwan Wee Tan,[†,⊥] David T. Moore,[†,⊥] Michael Saliba,[§,⊥] Hiroaki Sai,[†] Lara A. Estroff,[†] Tobias Hanrath,[‡] Henry J. Snaith,[§] and Ulrich Wiesner[†,*]

[†]Department of Materials Science and Engineering, [‡]School of Chemical and Biomolecular Engineering, Cornell University, Ithaca, New York 14853, United States and [§]Clarendon Laboratory, Department of Physics, University of Oxford, Oxford, OX1 3PU, U.K. [⊥]K. W. Tan, D. T. Moore, and M. Saliba contributed equally to this work.

ABSTRACT Structure control in solution-processed hybrid perovskites is crucial to design and fabricate highly efficient solar cells. Here, we utilize *in situ* grazing incidence wide-angle X-ray scattering and scanning electron microscopy to investigate the structural evolution and film morphologies of methylammonium lead tri-iodide/chloride ($CH_3NH_3PbI_{3-x}Cl_x$) in mesoporous block copolymer derived alumina superstructures during thermal annealing. We show the $CH_3NH_3PbI_{3-x}Cl_x$ material evolution to be characterized by three distinct structures: a crystalline precursor structure not described previously, a 3D perovskite structure, and a mixture of compounds resulting from degradation. Finally, we demonstrate how understanding the processing parameters provides the foundation needed for optimal perovskite film morphology and coverage, leading to enhanced block copolymer-directed perovskite solar cell performance.

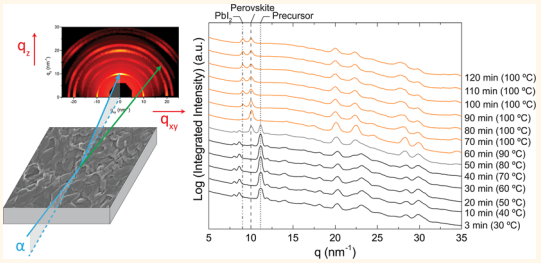

KEYWORDS: structural evolution · thermal annealing · self-assembly · block copolymer · hybrid perovskite · crystalline precursor · thin film solar cells

Harnessing sunlight to generate photovoltaic electricity based on thin film solar cell technologies is desirable to deliver green, sustainable energy at reduced materials and fabrication cost.[1,2] Thin film hybrid solar cells using solution-processable materials[2] such as semiconductor nanocrystals,[3,4] organic polymers,[5,6] or dye-sensitized solar cells[7−9] have achieved 7−12% power conversion efficiencies (PCEs). Recently, a new class of highly efficient solid-state hybrid perovskite solar cells has been reported pushing PCEs above 15%.[10−34]

Organic−inorganic hybrid materials enable the combination of both organic and inorganic qualities into a single molecular composite. These hybrid materials have been studied extensively for their electrical, mechanical, and optical functional properties and have been applied, for example, in field-effect transistors, optoelectronic devices, and hybrid solar cells.[35−38] Another area of intense scientific research and commercial interest is utilizing the methylammonium lead trihalide ($CH_3NH_3PbX_3$; X = I, Br, Cl) semiconducting perovskite in thin film photovoltaics.[10−34] The $CH_3NH_3PbX_3$ perovskite semiconductor material is highly attractive because of the ease of solution processing and excellent absorption properties in the near-infrared spectrum to generate charge carriers.[10,12,13,18] Moreover, ambipolar charge transport properties and long carrier lifetimes enable the direct transport of both photogenerated electron and hole charge carriers to the respective collecting electrodes.[14,15,18,19,28,29,34]

The photovoltaic device architecture provides an alternative approach to enhance device performance.[39−41] In particular, block copolymer (BCP) self-assembly directed materials have improved charge transport and light management of mesoscopic

* Address correspondence to ubw1@cornell.edu.

Received for review January 26, 2014 and accepted March 31, 2014.

Published online March 31, 2014
10.1021/nn500526t

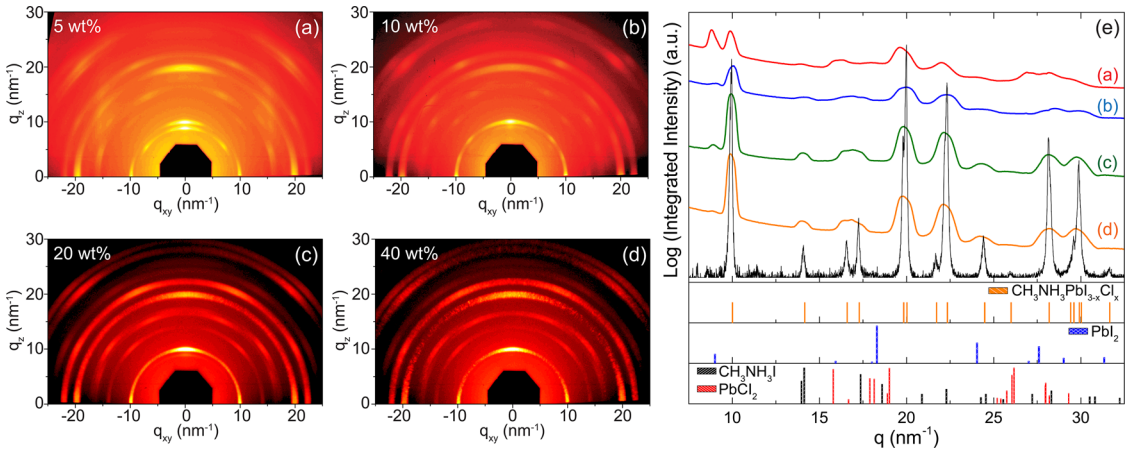

Figure 1. 2D GIWAXS profiles of $CH_3NH_3PbI_{3-x}Cl_x$ perovskite films on flat substrates prepared from (a) 5, (b) 10, (c) 20, and (d) 40 wt % precursor solutions and annealed at 100 °C for 45 min. (e) Azimuthally integrated intensity plots of the GIWAXS patterns. The bottom black curve is the XRD spectrum of the $CH_3NH_3PbI_{3-x}Cl_x$ perovskite measured in powdered form.

solar cells *via* control of morphology,[37,38,41−46] porosity and pore size,[46−50] material crystallinity,[51,52] electronic[37,52] and optical[47,53] properties. For example, well-ordered bicontinuous BCP gyroid morphologies enable easy backfilling of the hole transport materials and complete mesopore interconnectivity in solid-state dye-sensitized solar cells.[37,38] Moreover, porous BCP nanostructures provide control over single crystal epitaxial nanostructures[51] and may enable tuning the feature size and morphology of well-defined $CH_3NH_3PbX_3$ nanocrystallites within the BCP mesoporous heterojunction electrode to achieve excellent photovoltaic device performance.[19,24,32−34] Combining BCP structure control with the organic−inorganic hybrid perovskite, observation of structural evolution at multiple length scales is expected to be key to establishing structure−property correlations. To the best of our knowledge, such evolution of thermally annealed hybrid perovskites obtained *via* a single-step spin coating process has not been reported.

In this work we employed *in situ* time-resolved grazing incidence wide-angle X-ray scattering (GIWAXS) to probe the structure of methylammonium lead tri-iodide/chloride ($CH_3NH_3PbI_{3-x}Cl_x$) perovskites in mesoporous block copolymer-directed alumina (MBCP-Al_2O_3) during thermal annealing. Optimized structure and film morphology of the organic−inorganic hybrid perovskites resulted in enhanced meso-superstructured solar cell performance.

RESULTS AND DISCUSSION

GIWAXS of $CH_3NH_3PbI_{3-x}Cl_x$ Perovskites. One of the key advantages of the $CH_3NH_3PbX_3$ hybrid perovskite photovoltaic devices is the ease of solution-processing. The organic (CH_3NH_3I) and inorganic precursors ($PbCl_2$) are dissolved in a common solvent (*N*,*N*-dimethylformamide), deposited on a substrate by spin coating, and annealed at relatively low temperatures of 90−100 °C for 5−120 min to induce perovskite crystallization.[12−23,25−27] However, crystallographic data obtained from one-dimensional (1D) powder X-ray diffraction provides only limited structural information, in particular for the highly oriented perovskite thin films.[12,13,18,19,22−26] To this end, we employed GIWAXS with 2D detection capability to probe the crystallographic orientations of planar $CH_3NH_3PbI_{3-x}Cl_x$ perovskite thin films.

Figure 1 shows GIWAXS profiles of crystalline perovskite thin films on flat glass coverslips prepared from precursor solutions of different concentrations and annealed at 100 °C for 45 min in nitrogen atmosphere. We observe that the 5 and 10 wt % perovskite films exhibit a mixture of scattered secondary spots and rings (Figure 1a,b), indicating that crystalline domains are highly oriented in the in-plane direction. Similar GIWAXS profiles were observed for the thicker 20 and 40 wt % perovskite films. The presence of strongly scattered rings in Figure 1c,d indicates that crystalline domains are predominantly polycrystalline (*i.e.*, randomly oriented relative to the plane of the substrate). The azimuthally integrated scattering intensity of the different GIWAXS patterns is plotted against the scattering vector q in Figure 1e, where $q = 4\pi \sin\theta/\lambda$, θ is half of the total scattering angle, and λ is the X-ray wavelength (0.1161 nm). The 2D GIWAXS integrated intensity curves correspond well to the crystallographic peaks of the 1D X-ray diffraction pattern of a $CH_3NH_3PbI_{3-x}Cl_x$ powdered sample (black curve),[23] and are distinctly different from those of the CH_3NH_3I (PDF 00-10-0737) and $PbCl_2$ (PDF 00-050-0536) precursors (see bottom of Figure 1e). The lattice parameters for the tetragonal *I*4/*mcm* $CH_3NH_3PbI_{3-x}Cl_x$ powdered sample are a = 8.868(1) Å and c = 12.659(2) Å.[23,54−56] We note that while the broad GIWAXS scattering peaks do not allow precise structural assignments, distinct peaks observed for different species enable us to determine the predominant sample structure in real time. The scattering peak at

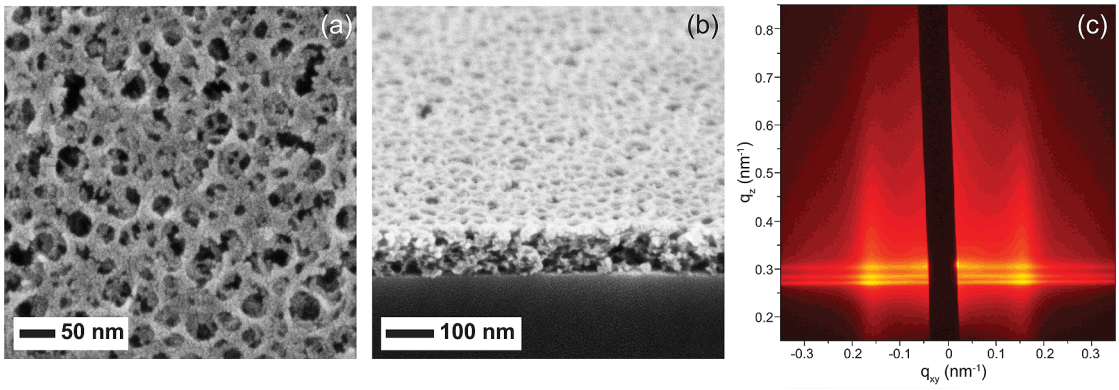

Figure 2. (a) Plan view and (b) cross-sectional SEM micrographs, and (c) 2D GISAXS profile at incidence angle of 0.16° of MBCP-Al_2O_3 film after calcination.

q = 10 nm^{-1} was assigned to the (110) plane of $CH_3NH_3PbI_{3-x}Cl_x$ perovskite structure.[18,23] The scattering peak at q = 9 nm^{-1} assigned to the (001) plane of PbI_2 (PDF 00-007-0235) was present only in the 5 wt % perovskite film, suggesting thinner films underwent a more rapid degradation into PbI_2.[13,23]

Characterization of Mesoporous Block Copolymer-Directed Alumina Thin Films. In a solvent mixture of nonpolar toluene and polar *n*-butanol, the structure directing poly(isoprene)-*block*-poly(styrene)-*block*-poly-(ethylene oxide) (PI-*b*-PS-*b*-PEO) triblock terpolymer forms micelles with the hydrophobic PI and PS in the core, and a hydrophilic PEO corona.[46−49] The added Al_2O_3 sol is selectively attracted to the PEO corona by hydrogen bonds.[42] Upon solvent evaporation, the organic−inorganic micelles self-assemble into a randomly packed arrangement. Mesoporous block copolymer-directed alumina (MBCP-Al_2O_3) thin films with interconnected porosity are generated when the organic components are removed by calcination as evidenced by the scanning electron microscopy (SEM) and atomic force microscopy (AFM) images in Figures 2 and S1 (Supporting Information), respectively. The MBCP-Al_2O_3 pores are interconnected in both in-plane and out-of-plane directions. From SEM and AFM, the pore diameter is ∼36 nm and the film thickness is 70−80 nm after calcination. In 2D grazing incidence small-angle X-ray scattering (GISAXS) patterns, we observe two intense diffraction peaks at $q_{xy} = \pm$ 0.157 nm^{-1} (Figure 2c) consistent with a disordered mesoporous material with a macroscopically homogeneous in-plane *d*-spacing of $2\pi/q_{xy} \approx$ 40 nm.[49] The oscillations at the diffraction peaks are attributed to the form factor of the film thickness.[57] In contrast, the porosity of Al_2O_3 nanoparticulate films is macroscopically inhomogeneous as shown in Figure S2 (Supporting Information).[18−20]

***In Situ* X-ray Characterization of MBCP-Al_2O_3 Perovskite Structural Evolution.** The mesoporous support in solution-processed nanostructured $CH_3NH_3PbX_3$ perovskite solar cells fulfills multiple roles. For example, mesoporous TiO_2 acts as the distributed heterojunction with large surface areas for the generation of charges by the $CH_3NH_3PbI_3$ perovskite absorber, and collects and transports the electrons to the collecting electrode.[10−17,24,32−34] Moreover, mesoporous superstructures improve the coating of perovskite material to enhance coverage and light harvesting efficiency,[19] and act as a physical barrier to prevent the formation of "shunt paths" by direct contact of the hole transport material and electron selective layer.[18−22] We applied *in situ* GIWAXS to study the structural evolution of solution-processed $CH_3NH_3PbI_{3-x}Cl_x$ perovskite on MBCP-Al_2O_3 thin films during annealing in real time.

As mentioned earlier, we observed similar GIWAXS patterns for the 20 and 40 wt % perovskite thin films (Figure 1c,d). Here we chose to deposit a 20 wt % perovskite precursor solution on the MBCP-Al_2O_3 thin film for isothermal-time-dependent (ITD) annealing in air and nitrogen, respectively. The precursor solution filled the interconnected mesopores and formed a "wet capping layer" on the superstructure scaffold with incomplete solvent removal. After deposition the sample was immediately loaded on a sample-stage held at 100 °C. It should be noted that in this way the ITD MBCP-Al_2O_3 perovskite samples underwent an immediate jump from ambient temperature to 100 °C. GIWAXS measurements were collected in real time over a dwell of 50 min. In the employed beam configuration, GIWAXS measured the perovskite material within the MBCP-Al_2O_3 scaffold and capping layer, as the incidence angle of the incoming X-ray beam was above the critical angle of the silicon substrate. *In situ* 2D GIWAXS profiles and azimuthally integrated intensity plots of the ITD MBCP-Al_2O_3 perovskite structural evolution in nitrogen and air, respectively, are shown in Figure 3.

For the study of the ITD MBCP-Al_2O_3 perovskite behavior in nitrogen, the wet sample was loaded into a custom-made environmental chamber on the heated stage at 100 °C under flowing nitrogen.[58] Under these conditions, the wet sample exhibits multiple orders of

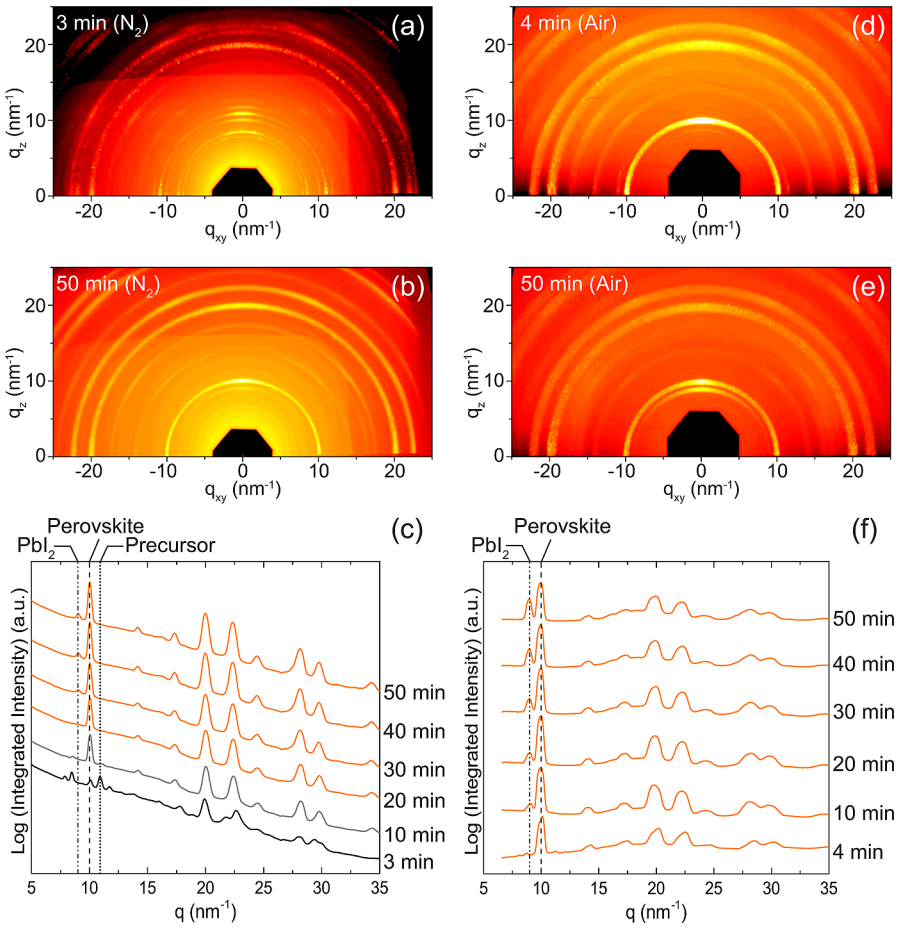

Figure 3. 2D GIWAXS profiles for ITD annealing of MBCP-Al_2O_3 perovskite films at 100 °C in (a,b) nitrogen and (d,e) air for different time points as indicated, together with (c,f) respective azimuthally integrated intensity plots. The dotted line at $q \approx 11$ nm^{-1}, dashed line at $q = 10$ nm^{-1}, and dash-dotted line at $q = 9$ nm^{-1} denote the signature scattering peaks for the crystalline precursor, perovskite, and PbI_2 structures, respectively.

scattering rings in the GIWAXS profile (Figure 3a), indicating the formation of crystalline material. Interestingly, from the integrated intensity plots in Figure 3c, at short times (3 min time point) we observe a distinct set of scattering peaks at lower q values (<9 nm^{-1}) that are neither characteristic for CH_3NH_3I, $PbCl_2$, PbI_2, nor for the $CH_3NH_3PbI_{3-x}Cl_x$ perovskite structure. After 10 min the expected peaks for the mixed halide perovskite are observed (compare Figure 3c with Figure 1e). This observation suggests the formation of a distinct crystalline structure, which in the following discussion we will refer to as the "crystalline precursor structure". We assigned the peak at $q \approx 11$ nm^{-1} as the signature scattering peak for this crystalline precursor structure. Further investigation is currently underway to identify the structure of this crystalline precursor material. Somewhere between 3 and 10 min of annealing in nitrogen under the set conditions, the film underwent a transition to form the mixed halide perovskite structure, at which point the intensity of the peak at $q \approx 11$ nm^{-1} for the crystalline precursor in Figure 3c vanishes. The film started to degrade into PbI_2 after about 20−30 min of annealing, as indicated by the appearance of a scattering peak at $q = 9$ nm^{-1}. The degradation may be attributed to the presence of moisture in the chamber,[13,22,23,54,56] but at this point X-ray beam induced damage cannot be excluded either. For comparison, Figure 3b shows the GIWAXS profile of the MBCP-Al_2O_3 perovskite film after 50 min annealing in nitrogen at 100 °C.

From the beginning of ITD annealing at 100 °C in air, we observe multiple orders of scattering rings in the GIWAXS profile (Figure 3d), consistent with the rapid formation of a polycrystalline perovskite phase in the presence of MBCP-Al_2O_3. Figure 3f shows the azimuthally integrated intensity plot of the ITD experiments in air with the perovskite signature peak at $q = 10$ nm^{-1}. Within 10 min at 100 °C, the perovskite started to degrade to PbI_2 as signified by the new peak formed at $q = 9$ nm^{-1}. The degradation is likely to initiate from the perovskite film surface[56] and may be attributed to moisture in the air[13,22,23,54] and X-ray beam induced damage. Over the dwell of 50 min at 100 °C, the scattering peaks remained in the same positions as shown in Figure 3e,f, suggesting minimal reorientation changes to the perovskite structure. Under air the

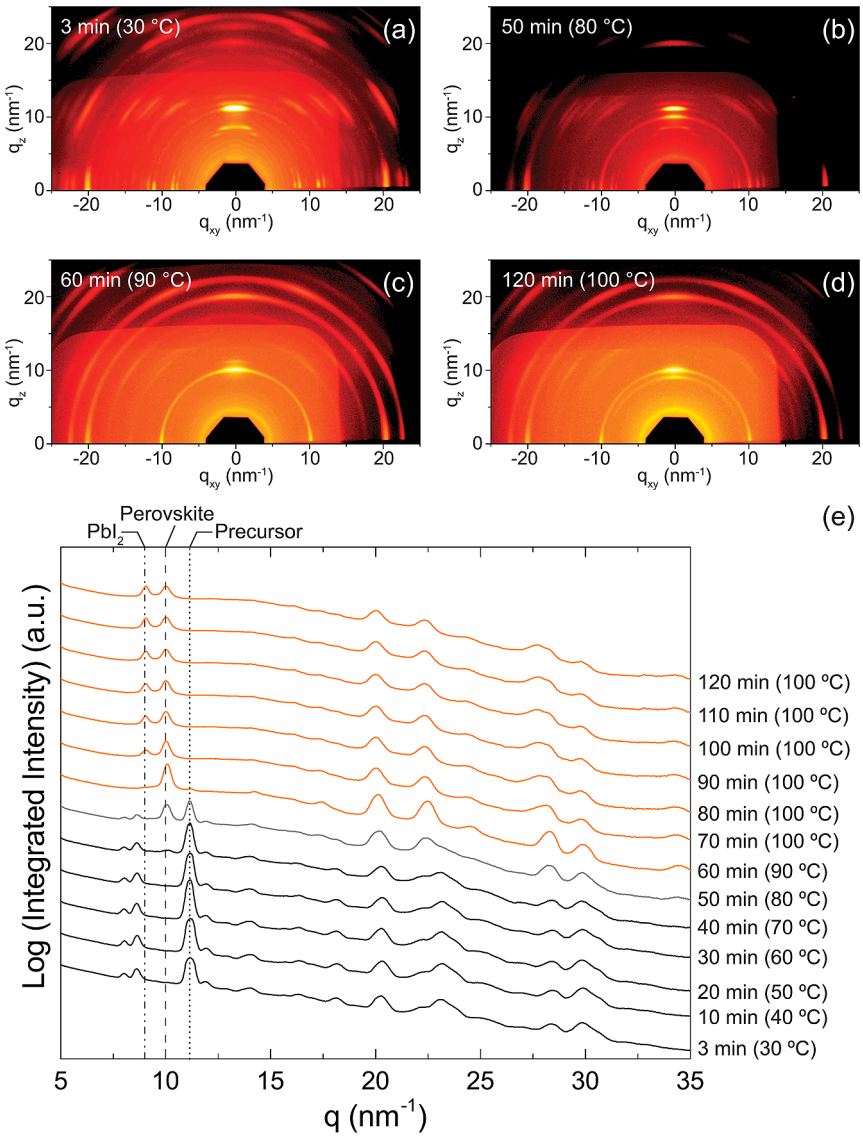

Figure 4. 2D GIWAXS profiles for TTD annealing of MBCP-Al_2O_3 perovskite films in nitrogen after (a) 3, (b) 50, (c) 60, and (d) 120 min, together with (e) azimuthally integrated intensity plots. The dotted line at $q \approx 11$ nm^{-1}, dashed line at $q = 10$ nm^{-1}, and dash-dotted line at $q = 9$ nm^{-1} denote the signature scattering peaks for the crystalline precursor, perovskite, and PbI_2 structures, respectively. The difference in background brightness of the GIWAXS patterns is a shadow artifact of the experimental setup.

perovskite structure already showed first indications of degradation *via* the peak at $q = 9$ nm^{-1} by the 10 min time point. We suspect that the absence of the crystalline precursor structure may be due to a more rapid transition in air as compared to nitrogen. We observe similar behavior, *i.e.*, the absence of the crystalline precursor for $CH_3NH_3PbI_{3-x}Cl_x$ on a MBCP-TiO_2 superstructure annealed in air, albeit with more severe degradation into PbI_2 (Figure S3, Supporting Information).

To delineate how individual parameters contribute to the structural evolution of $CH_3NH_3PbI_{3-x}Cl_x$ on MBCP-Al_2O_3, we conducted time−temperature-dependent (TTD) GIWAXS measurements with a slow temperature ramp applied to the wet MBCP-Al_2O_3 perovskite sample in nitrogen. To that end, 20 wt % precursor solution was deposited on the MBCP-Al_2O_3 thin film and loaded into the environmental chamber held at 30 °C under flowing nitrogen. The temperature of the heating stage was raised by 10 °C at every 10 min time interval. It took approximately 2−3 min for the heated stage to reach the set temperature. Figure 4 displays four representative 2D GIWAXS profiles (Figure 4a−d), while the integrated intensity plots (Figure 4e) reveal the TTD structural evolution of the MBCP-Al_2O_3 perovskite sample from 30 to 100 °C over the dwell of 120 min.

At the beginning of the experiment, the crystalline precursor was detected in the GIWAXS profile *via* the peak at $q \approx 11$ nm^{-1}; see also GIWAXS pattern in Figure 4a showing results for the 3 min (30 °C) time point. At the 50 min time point (80 °C) a scattering ring

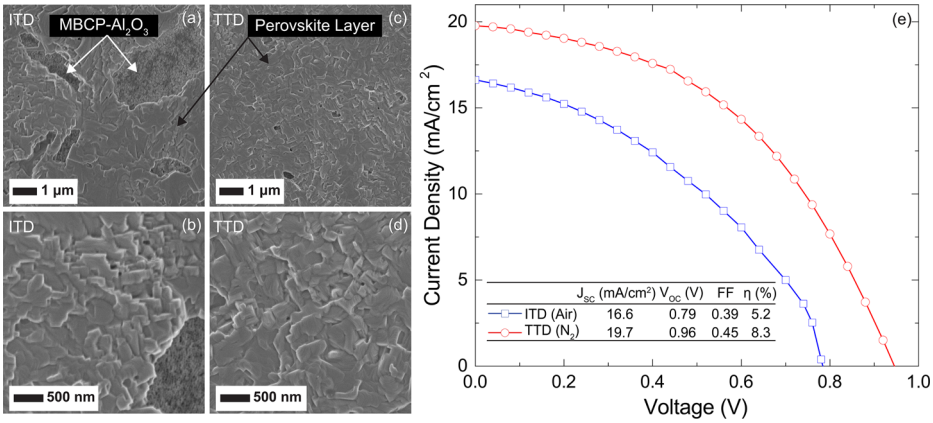

Figure 5. Plan view SEM micrographs of perovskite crystallization in MBCP-Al_2O_3 annealed under (a,b) ITD and (c,d) TTD conditions in nitrogen. (e) Current density/voltage curves of best performing MBCP-Al_2O_3 perovskite solar cells measured under stimulated AM1.5 sunlight of 100 mW/cm^2 irradiation for different annealing conditions (ITD *versus* TTD).

appeared at q = 10 nm^{-1} (Figure 4b), indicating the transition from the crystalline precursor to polycrystalline perovskite. This structural transition was completed at the 60 min time point (90 °C, Figure 4c), similar to the 10 min time point for the ITD annealed MBCP-Al_2O_3 perovskite at 100 °C in nitrogen (compare with Figure 3c). Perovskite film degradation was observed at the 70 min time point after the temperature was raised to the final value of 100 °C, and progressed until the final time point at 120 min (Figure 4d). Similar to the ITD annealing in nitrogen, three distinct structures were identified during the TTD processing of $CH_3NH_3PbI_{3-x}Cl_x$ in MBCP-Al_2O_3 superstructures: (1) crystalline precursor, (2) perovskite, and (3) PbI_2 as a perovskite degradation product.

From the present and previous work, we conclude that transitions between these different structures are driven by a combination of annealing temperature, environmental atmosphere and film thickness.[22,26,27] A yet-to-be identified crystalline precursor structure was observed upon spin coating the $CH_3NH_3PbI_{3-x}Cl_x$ precursor solution on MBCP-Al_2O_3, and displayed noteworthy thermal stability during the TTD ramp annealing. We postulate that the crystalline precursor undergoes a solid−solid phase transformation to the 3D perovskite structure at 80 °C. This transition occurs relatively rapidly (<10 min) and is largely completed at 90 °C. To the best of our knowledge, this is the first experimental observation of a transformation from a crystalline precursor to the perovskite crystal structure for methylammonium lead trihalide perovskite materials, suggesting a phase transformation pathway consistent with Ostwald's "Rule of Stages" in which a metastable precursor is first formed, followed by transformation into the more stable product.[59,60]

We further note that macroscopic coverage of the substrate with perovskite layers is largely affected by the heat treatment profile. In plan view SEM images (Figure S4a,b, Supporting Information) we observe large (>2 μm) perovskite crystallite islands and pores in the capping layer on MBCP-Al_2O_3 under ITD annealing conditions. In contrast, the discrete perovskite islands and pores are on the submicrometer length scale for the TTD annealed MBCP-Al_2O_3 perovskite film shown in Figure S4d,e (Supporting Information). Since the only difference in the heat treatment profile is at the initial stage before perovskite formation, this result suggests that the crystalline precursor coverage and the subsequent phase transformation contributes significantly to the final film coverage, which in turn greatly affects device performance (*vide infra*).

MBCP-Al_2O_3 Perovskite Solar Cell Performance. Figure 5 shows SEM images of MBCP-Al_2O_3 perovskite films prepared from 40 wt % precursor solutions and annealed either instantaneously at 100 °C (ITD), or with a slow temperature ramp to 100 °C (TTD) in nitrogen. While the crystallite domain sizes are very similar for the ITD and TTD annealed films (Figure 5c,d), the capping film coverage is drastically different. Figure 5a shows that large pores (>1 μm) were formed in the capping layer of the MBCP-Al_2O_3 perovskite films annealed instantly at 100 °C (ITD). In contrast, when the MBCP-Al_2O_3 perovskite film was annealed with a slow temperature ramp of 5 °C/5 min in nitrogen to 100 °C and held for 45 min at the final temperature (TTD), significantly better perovskite film coverage was achieved. The 40 wt % perovskite film morphology is highly similar to the 20 wt % perovskite films (Figure S4, Supporting Information). We hypothesize that the crystalline precursor, which is present for a longer dwell period during TTD annealing, promotes film formation with fewer macroscopic defects than in ITD annealed films.

We fabricated MBCP-Al_2O_3 perovskite solar cells annealed under ITD and TTD conditions (see Table S1, Supporting Information). Comparing the best performing MBCP-Al_2O_3 perovskite solar cells in Figure 5e, the values of short-circuit current density (J_{SC}), open-circuit voltage (V_{OC}), and fill factor (FF) of the TTD-N_2 device increased by at least 15% relative to the ITD-air device.

At the same time, the power conversion efficiency increased from 5.2 to 8.3%. We attribute the device performance improvement to the enhanced perovskite film morphology and coverage, enabling more uniform charge generation and collection, and reduced leakage with fewer available shunt paths.[19,22,26,27]

CONCLUSION

In conclusion, we employed *in situ* 2D GIWAXS in combination with SEM to follow the structural evolution of $CH_3NH_3PbI_{3-x}Cl_x$ perovskite on mesoporous block copolymer Al_2O_3 thin films under thermal annealing. Solution-processed perovskite films underwent transitions between three distinct crystalline structures during thermal annealing: a crystalline precursor, a perovskite, and a degradation product in the form of PbI_2. Finally, we demonstrated by annealing the MBCP-Al_2O_3 perovskite films with a well-controlled temperature ramp in a dry environment that the perovskite capping film coverage and the power conversion efficiency of block copolymer-directed alumina perovskite solar cells can be greatly improved. To the best of our knowledge, the crystalline precursor has not previously been described, and its exact structure is currently unknown. We showed that the evolution between these structures markedly depends on the annealing conditions. A clear understanding of $CH_3NH_3PbX_3$ wet solution processing conditions in combination with bicontinuous BCP gyroidal titania electrodes[37,38] with an interconnecting pore network may allow complete perovskite infiltration, and enhance the photogenerated electron collection and transport for optimal solar cell performance.[24,32−34]

METHODS

Materials. All materials were used as received. Anhydrous grades of toluene, *n*-butanol, tetrahydrofuran, chloroform, *N*,*N*-dimethylformamide and terpineol, 97% aluminum tri-*sec*-butoxide, >97% titanium isopropoxide, 20 wt % aluminum oxide nanoparticles in isopropanol (<50 nm, product number 702129), 57 wt % hydriodic acid in water, 33 wt % methylamine solution in ethanol, and lead chloride were obtained from Sigma-Aldrich. 70% nitric acid and 37% hydrochloric acid were obtained from Mallinckrodt Baker and EMD Millipore, respectively. 10 and 46 cP ethyl cellulose were obtained from TCI America.

Mesoporous Block Copolymer-Directed Alumina (MBCP-Al_2O_3) and Titania (MBCP-TiO_2) Films. MBCP-Al_2O_3 thin films were prepared using 50 mg of poly(isoprene)-*block*-poly(styrene)-*block*-poly(ethylene oxide) (ISO, M_n = 38.3 kg/mol, with a polydispersity index of 1.07 containing 68.4 wt % PI and 18.0 wt % PS) dissolved in 500 mg of toluene and *n*-butanol solvent mixture (1:1, w/w). In a separate vial, 104 mg of 97% aluminum tri-*sec*-butoxide, 478 mg of *n*-butanol, and 478 mg of toluene were added sequentially. The white cloudy suspension was left undisturbed for 15 min, followed by vigorous stirring for 30 min to allow homogenization. 55 μL of 70% nitric acid was added, and the mixture was stirred overnight (>12 h). The transparent alumina sol was added into the ISO solution and stirred for 45 min. The ISO-Al_2O_3 solution was processed by spin coating on silicon at 2000 rpm (45 s) in a nitrogen drybox. The MBCP-Al_2O_3 hybrid thin films were baked at 50 °C (2 h), 100 °C (2 h), and 130 °C (2 h) sequentially in the drybox and calcined in a tube furnace at 450 °C (3 h) with a ramp rate of 1 °C/min.

MBCP-TiO_2 thin films were prepared using a modified method as described elsewhere.[38] Briefly, 50 mg of ISO was dissolved in 1.35 g of tetrahydrofuran and chloroform solvent mixture (4:5, w/w). In a separate vial, 53.9 μL of >97% titanium isopropoxide, 16.8 μL of 37% HCl acid, and 216 μL of tetrahydrofuran were mixed and stirred vigorously. The yellow-colored titania sol was added into the ISO solution and stirred for 45 min. The ISO-TiO_2 solution was processed by spin coating on silicon at 2000 rpm (45 s) in the drybox. The MBCP-TiO_2 hybrid thin films were baked at 50 °C (2 h), 100 °C (2 h), and calcined in a tube furnace at 450 °C (3 h) with a ramp rate of 1 °C/min.

Mesoporous Alumina Nanoparticle (NP) Films. Mesoporous Al_2O_3 nanoparticle (NP) thin films were prepared as described elsewhere.[18−20] The binder-free mesoporous Al_2O_3 NP film was prepared by spin coating 6.67 wt % Al_2O_3 NPs in isopropanol on silicon at 2500 rpm (60 s), and baked at 150 °C (1 h). The 2 wt % Al_2O_3 NP-binder paste was prepared by mixing 1 g of Al_2O_3 NPs, 3.33 g of terpineol, 1 g of 10 cP ethyl cellulose and 1 g of 46 cP ethyl cellulose in 43.67 g of isopropanol. The mixture was stirred vigorously at 70 °C for 30 min. The mesoporous Al_2O_3 NP film with binder was prepared by spin coating the Al_2O_3 NP-binder mixture on silicon at 2500 rpm (60 s) and calcined in a tube furnace at 500 °C (3 h) with a ramp rate of 1 °C/min.

Mesoporous Alumina Thin Film Characterization. Scanning electron microscopy (SEM) images were acquired on Au−Pd coated mesoporous alumina thin films using LEO 1550 and TESCAN MIRA3-LM field emission SEMs equipped with in-lens detectors. Atomic force microscopy (AFM) images were obtained on a Veeco Multimode II SPM with a Nanoscope III controller in tapping mode at ambient conditions. GISAXS was measured at the G1 beamline of the Cornell High Energy Synchrotron Source (CHESS). The G1 beamline setup consists of a multilayer monochromator of wavelength λ = 0.1225 nm with a CCD area detector with a 71.73 μm pixel size and a total of 1024 × 1024 pixels. The sample-to-detector distance was 2.745 m. The incident angle of the beam was varied between 0.1° and 0.3° with typical exposure times <2 s. GISAXS patterns were analyzed with an in-house software[61] and the FIT2D program.[62]

Wide-Angle X-ray Scattering Measurements of Methylammonium Lead Tri-iodide/Chloride Hybrid Perovskite. Methylammonium iodide (CH_3NH_3I) was prepared using 57 wt % hydriodic acid (HI) in water and 33 wt % methylamine solution (CH_3NH_2) in ethanol as reported elsewhere.[18] 5−40 wt % of methylammonium iodide (CH_3NH_3I) and lead chloride ($PbCl_2$) (3:1 by molarity) dissolved in *N*,*N*-dimethylformamide was dispensed on the MBCP-Al_2O_3 and flat glass coverslip substrates by spin coating at 3000 rpm (45 s) in air. For *ex situ* measurements, the hybrid perovskite samples were annealed by a slow temperature ramp of 10 °C/10 min and held at 100 °C for 45 min in a nitrogen atmosphere. The annealed perovskite films were carefully scratched from the substrate and powdered for X-ray diffraction (XRD) analysis. The XRD characterization was performed on a Rigaku Ultima IV multipurpose X-ray diffraction system using Cu Kα radiation (40 kV, 44 mA, wavelength λ = 1.5418 Å) and unit cell refinement analysis with the MDI Jade 9 software.

For *in situ* GIWAXS measurements, after spin coating the sample was immediately loaded on a temperature-controlled stage at the D1 beamline of CHESS. The D1 beamline setup consists of a multilayer monochromator of wavelength λ = 0.1161 nm. GIWAXS patterns were collected on Fuji image plates placed in a holder at a distance of 177 mm from the sample. The incident beam angle was above the silicon critical angle (~0.25°) with exposure times <5 s. The direct beam was blocked with lead tape. The exposed plates were scanned for digital processing with a GE Healthcare Typhoon FLA-7000

image plate reader. Digital images were analyzed using the FIT2D program.[62] The resolution of the letter-sized image plate is 2000 × 2500 pixels with a 100 μm pixel size. The measurements in nitrogen were conducted in a custom-made environmental chamber mounted on the temperature-controlled stage.[58]

Isothermal-Time-Dependent (ITD) Perovskite Crystallization. A 20 wt % precursor solution was dispensed on the MBCP-Al_2O_3 substrate by spin coating and immediately loaded on the temperature-stage held at 100 °C at the D1 beamline. GIWAXS measurements were taken at different time intervals over a dwell of 50 min. The measurements were conducted in ambient air and nitrogen.

Time−Temperature-Dependent (TTD) Perovskite Crystallization. A 20 wt % precursor solution was dispensed on the MBCP-Al_2O_3 substrate by spin coating and loaded on the temperature-stage held at 30 °C at the D1 beamline. The stage was slowly heated at a ramp rate of 10 °C/10 min to the final temperature of 100 °C. The MBCP-Al_2O_3 perovskite sample was held at 100 °C for 60 min. The GIWAXS measurements were taken at different time intervals in nitrogen.

MBCP-Al_2O_3 Hybrid Perovskite Solar Cell Assembly. MBCP-Al_2O_3 perovskite solar cells (>20 cells for each annealing history) were fabricated as reported elsewhere.[18] Briefly, HCl-etched FTO glass substrates were coated with a dense TiO_2 compact layer prepared by spin coating a mildly HCl-acidified solution of titanium isopropoxide in ethanol, and sintered at 500 °C for 45 min. The MBCP-Al_2O_3 hybrid films were prepared by spin coating on the TiO_2/FTO substrates at 2000 rpm (45 s). The substrates were baked at 50 °C (2 h), 100 °C (2 h), and 130 °C (2 h) sequentially in the drybox and calcined at 450 °C (3 h) with a ramp rate of 1 °C/min.

A 40 wt % perovskite precursor solution was dispensed on the MBCP-Al_2O_3 scaffold by spin coating at 2000 rpm (45 s). For the ITD-air processed MBCP-Al_2O_3 perovskite solar cells, the devices were fabricated in ambient air and heated in an oven at 100 °C for 45 min. For the TTD-nitrogen processed MBCP-Al_2O_3 perovskite solar cells, the devices were fabricated in a nitrogen glovebox. After drying at ambient temperature for at least 20 min, the samples were slowly heated on a hot plate from ambient temperature to 100 °C at a ramp rate of 5 °C/5 min, and held at 100 °C for 45 min. The electron blocking layer was formed by spin coating 80 mM 2,2′,7,7′-tetrakis(*N*,*N*-di-*p*-methoxyphenylamine)-9,9′-spirobifluorene (spiro-OMeTAD) in chlorobenzene solution with 68.3 mM *tert*-butylpyridine and 22.6 mM lithium bis(trifluoromethanesulfonyl)imide additives (170 mg/mL in acetonitrile) and aged overnight in a desiccator (in air). Silver contact electrodes of 150 nm were thermally evaporated to complete the devices.

MBCP-Al_2O_3 Hybrid Perovskite Solar Cell Characterization. More than 20 solar cells were measured for each annealing condition (ITD *versus* TTD) with a Keithley 2400 under AM 1.5G 100 mW/cm^2 simulated sunlight (Abet Technologies Sun 2000) calibrated against an NREL certified KG5 filtered silicon reference diode. The cells were masked with a square aperture defining an active area of typically 0.07 cm^2 and measured in a light-tight sample holder.

Conflict of Interest: The authors declare no competing financial interest.

Acknowledgment. The authors acknowledge financial support from the National Science Foundation (NSF) through the Materials World Network grant between the U.S. (DMR-1008125) and the U.K. (Engineering and Physical Sciences Research Council, EPSRC). K.W.T. gratefully acknowledges the Singapore Energy Innovation Programme Office for a National Research Foundation graduate fellowship. This work made use of the research facilities of the Cornell Center for Materials Research (CCMR) with support from the NSF Materials Research Science and Engineering Centers (MRSEC) program (DMR-1120296), Cornell High Energy Synchrotron Source (CHESS), which is supported by the NSF and the NIH/National Institute of General Medical Sciences under NSF Award DMR-0936384, and the KAUST-Cornell Center for Energy and Sustainability supported by Award No. KUS-C1-018-02, made by King Abdullah University of Science and Technology (KAUST). The authors gratefully acknowledge D. M. Smilgies, M. Koker, R. Li, J. Kim, S. W. Robbins, T. Scott, and J. Song of Cornell University for kind experimental assistance.

Supporting Information Available: Additional atomic force microscopy, scanning electron microscopy, grazing incidence wide-angle and small-angle X-ray scattering characterization, and device performance. This material is available free of charge *via* the Internet at http://pubs.acs.org.

Note Added in Proof: During the revision of this paper, a highly relevant article on this topic was published: Dualeh, A.; Tétreault, N.; Moehl, T.; Gao, P.; Nazeeruddin, M. K.; Grätzel, M. Effect of Annealing Temperature on Film Morphology of Organic-Inorganic Hybrid Pervoskite Solid-State Solar Cells. *Adv. Funct. Mater.* **2014**, DOI: 10.1002/adfm.201304022.

REFERENCES AND NOTES

1. Cho, A. Energy's Tricky Tradeoffs. *Science* **2010**, *329*, 786–787.
2. Graetzel, M.; Janssen, R. A. J.; Mitzi, D. B.; Sargent, E. H. Materials Interface Engineering for Solution-Processed Photovoltaics. *Nature* **2012**, *488*, 304–312.
3. Ip, A. H.; Thon, S. M.; Hoogland, S.; Voznyy, O.; Zhitomirsky, D.; Debnath, R.; Levina, L.; Rollny, L. R.; Carey, G. H.; Fischer, A.; *et al.* Hybrid Passivated Colloidal Quantum Dot Solids. *Nat. Nanotechnol.* **2012**, *7*, 577–582.
4. Ning, Z.; Zhitomirsky, D.; Adinolfi, V.; Sutherland, B.; Xu, J.; Voznyy, O.; Maraghechi, P.; Lan, X.; Hoogland, S.; Ren, Y.; *et al.* Graded Doping for Enhanced Colloidal Quantum Dot Photovoltaics. *Adv. Mater.* **2013**, *25*, 1719–1723.
5. Service, R. F. Outlook Brightens for Plastic Solar Cells. *Science* **2011**, *332*, 293–293.
6. You, J.; Dou, L.; Yoshimura, K.; Kato, T.; Ohya, K.; Moriarty, T.; Emery, K.; Chen, C.-C.; Gao, J.; Li, G.; *et al.* A Polymer Tandem Solar Cell with 10.6% Power Conversion Efficiency. *Nat. Commun.* **2013**, *4*, 1446.
7. Yella, A.; Lee, H.-W.; Tsao, H. N.; Yi, C.; Chandiran, A. K.; Nazeeruddin, M. K.; Diau, E. W.-G.; Yeh, C.-Y.; Zakeeruddin, S. M.; Grätzel, M. Porphyrin-Sensitized Solar Cells with Cobalt (II/III)-Based Redox Electrolyte Exceed 12 Percent Efficiency. *Science* **2011**, *334*, 629–634.
8. Han, L.; Islam, A.; Chen, H.; Malapaka, C.; Chiranjeevi, B.; Zhang, S.; Yang, X.; Yanagida, M. High-Efficiency Dye-Sensitized Solar Cell with a Novel Co-Adsorbent. *Energy Environ. Sci.* **2012**, *5*, 6057–6060.
9. Chung, I.; Lee, B.; He, J.; Chang, R. P. H.; Kanatzidis, M. G. All-Solid-State Dye-Sensitized Solar Cells with High Efficiency. *Nature* **2012**, *485*, 486–489.
10. Kojima, A.; Teshima, K.; Shirai, Y.; Miyasaka, T. Organometal Halide Perovskites as Visible-Light Sensitizers for Photovoltaic Cells. *J. Am. Chem. Soc.* **2009**, *131*, 6050–6051.
11. Im, J.-H.; Lee, C.-R.; Lee, J.-W.; Park, S.-W.; Park, N.-G. 6.5% Efficient Perovskite Quantum-Dot-Sensitized Solar Cell. *Nanoscale* **2011**, *3*, 4088–4093.
12. Kim, H.-S.; Lee, C.-R.; Im, J.-H.; Lee, K.-B.; Moehl, T.; Marchioro, A.; Moon, S.-J.; Humphry-Baker, R.; Yum, J.-H.; Moser, J. E.; *et al.* Lead Iodide Perovskite Sensitized All-Solid-State Submicron Thin Film Mesoscopic Solar Cell with Efficiency Exceeding 9%. *Sci. Rep.* **2012**, *2*, 591.
13. Noh, J. H.; Im, S. H.; Heo, J. H.; Mandal, T. N.; Seok, S. I. Chemical Management for Colorful, Efficient, and Stable Inorganic−Organic Hybrid Nanostructured Solar Cells. *Nano Lett.* **2013**, *13*, 1764–1769.
14. Etgar, L.; Gao, P.; Xue, Z.; Peng, Q.; Chandiran, A. K.; Liu, B.; Nazeeruddin, M. K.; Grätzel, M. Mesoscopic $CH_3NH_3PbI_3$/TiO_2 Heterojunction Solar Cells. *J. Am. Chem. Soc.* **2012**, *134*, 17396–17399.
15. Heo, J. H.; Im, S. H.; Noh, J. H.; Mandal, T. N.; Lim, C.-S.; Chang, J. A.; Lee, Y. H.; Kim, H.; Sarkar, A.; Nazeeruddin, M. K.; *et al.* Efficient Inorganic-Organic Hybrid Heterojunction Solar Cells Containing Perovskite Compound and Polymeric Hole Conductors. *Nat. Photonics* **2013**, *7*, 486–491.
16. Crossland, E. J. W.; Noel, N.; Sivaram, V.; Leijtens, T.; Alexander-Webber, J. A.; Snaith, H. J. Mesoporous TiO_2

Single Crystals Delivering Enhanced Mobility and Optoelectronic Device Performance. *Nature* **2013**, *495*, 215–219.
17. Kim, H.-S.; Mora-Sero, I.; Gonzalez-Pedro, V.; Fabregat-Santiago, F.; Juarez-Perez, E. J.; Park, N.-G.; Bisquert, J. Mechanism of Carrier Accumulation in Perovskite Thin-Absorber Solar Cells. *Nat. Commun.* **2013**, *4*, 2242.
18. Lee, M. M.; Teuscher, J.; Miyasaka, T.; Murakami, T. N.; Snaith, H. J. Efficient Hybrid Solar Cells Based on Meso-Superstructured Organometal Halide Perovskites. *Science* **2012**, *338*, 643–647.
19. Ball, J. M.; Lee, M. M.; Hey, A.; Snaith, H. J. Low-Temperature Processed Meso-Superstructured to Thin-Film Perovskite Solar Cells. *Energy Environ. Sci.* **2013**, *6*, 1739–1743.
20. Edri, E.; Kirmayer, S.; Cahen, D.; Hodes, G. High Open-Circuit Voltage Solar Cells Based on Organic–Inorganic Lead Bromide Perovskite. *J. Phys. Chem. Lett.* **2013**, 897–902.
21. Zhang, W.; Saliba, M.; Stranks, S. D.; Sun, Y.; Shi, X.; Wiesner, U.; Snaith, H. J. Enhancement of Perovskite-Based Solar Cells Employing Core–Shell Metal Nanoparticles. *Nano Lett.* **2013**, *13*, 4505–4510.
22. Eperon, G. E.; Burlakov, V. M.; Docampo, P.; Goriely, A.; Snaith, H. J. Morphological Control for High Performance, Solution-Processed Planar Heterojunction Perovskite Solar Cells. *Adv. Funct. Mater.* **2014**, *24*, 151–157.
23. Colella, S.; Mosconi, E.; Fedeli, P.; Listorti, A.; Gazza, F.; Orlandi, F.; Ferro, P.; Besagni, T.; Rizzo, A.; Calestani, G.; *et al.* $MAPbI_{3-x}Cl_x$ Mixed Halide Perovskite for Hybrid Solar Cells: The Role of Chloride as Dopant on the Transport and Structural Properties. *Chem. Mater.* **2013**, *25*, 4613–4618.
24. Burschka, J.; Pellet, N.; Moon, S.-J.; Humphry-Baker, R.; Gao, P.; Nazeeruddin, M. K.; Grätzel, M. Sequential Deposition as a Route to High-Performance Perovskite-Sensitized Solar Cells. *Nature* **2013**, *499*, 316–319.
25. Liu, M.; Johnston, M. B.; Snaith, H. J. Efficient Planar Heterojunction Perovskite Solar Cells by Vapour Deposition. *Nature* **2013**, *501*, 395–398.
26. Conings, B.; Baeten, L.; De Dobbelaere, C.; D'Haen, J.; Manca, J.; Boyen, H.-G. Perovskite-Based Hybrid Solar Cells Exceeding 10% Efficiency with High Reproducibility Using a Thin Film Sandwich Approach. *Adv. Mater.* **2013**, 10.1002/adma.201304803.
27. Jeng, J.-Y.; Chiang, Y.-F.; Lee, M.-H.; Peng, S.-R.; Guo, T.-F.; Chen, P.; Wen, T.-C. $CH_3NH_3PbI_3$ Perovskite/Fullerene Planar-Heterojunction Hybrid Solar Cells. *Adv. Mater.* **2013**, *25*, 3727–3732.
28. Stranks, S. D.; Eperon, G. E.; Grancini, G.; Menelaou, C.; Alcocer, M. J. P.; Leijtens, T.; Herz, L. M.; Petrozza, A.; Snaith, H. J. Electron-Hole Diffusion Lengths Exceeding 1 Micrometer in an Organometal Trihalide Perovskite Absorber. *Science* **2013**, *342*, 341–344.
29. Xing, G.; Mathews, N.; Sun, S.; Lim, S. S.; Lam, Y. M.; Grätzel, M.; Mhaisalkar, S.; Sum, T. C. Long-Range Balanced Electron- and Hole-Transport Lengths in Organic-Inorganic $CH_3NH_3PbI_3$. *Science* **2013**, *342*, 344–347.
30. Liu, D.; Kelly, T. L. Perovskite Solar Cells with a Planar Heterojunction Structure Prepared Using Room-Temperature Solution Processing Techniques. *Nat. Photonics* **2014**, *8*, 133–138.
31. You, J.; Hong, Z.; Yang, Y. M.; Chen, Q.; Cai, M.; Song, T.-B.; Chen, C.-C.; Lu, S.; Liu, Y.; Zhou, H.; *et al.* Low-Temperature Solution-Processed Perovskite Solar Cells with High Efficiency and Flexibility. *ACS Nano* **2014**, *8*, 1674–1680.
32. Edri, E.; Kirmayer, S.; Henning, A.; Mukhopadhyay, S.; Gartsman, K.; Rosenwaks, Y.; Hodes, G.; Cahen, D. Why Lead Methylammonium Tri-Iodide Perovskite-Based Solar Cells Require a Mesoporous Electron Transporting Scaffold (but Not Necessarily a Hole Conductor). *Nano Lett.* **2014**, *14*, 1000–1004.
33. Gonzalez-Pedro, V.; Juarez-Perez, E. J.; Arsyad, W.-S.; Barea, E. M.; Fabregat-Santiago, F.; Mora-Sero, I.; Bisquert, J. General Working Principles of $CH_3NH_3PbX_3$ Perovskite Solar Cells. *Nano Lett.* **2014**, *14*, 888–893.
34. Marchioro, A.; Teuscher, J.; Friedrich, D.; Kunst, M.; van de Krol, R.; Moehl, T.; Grätzel, M.; Moser, J.-E. Unravelling the Mechanism of Photoinduced Charge Transfer Processes in Lead Iodide Perovskite Solar Cells. *Nat. Photonics* **2014**, *8*, 250–255.
35. Kagan, C. R.; Mitzi, D. B.; Dimitrakopoulos, C. D. Organic-Inorganic Hybrid Materials as Semiconducting Channels in Thin-Film Field-Effect Transistors. *Science* **1999**, *286*, 945–947.
36. Mitzi, D. B.; Chondroudis, K.; Kagan, C. R. Organic–Inorganic Electronics. *IBM J. Res. Dev.* **2001**, *45*, 29–45.
37. Crossland, E. J. W.; Kamperman, M.; Nedelcu, M.; Ducati, C.; Wiesner, U.; Smilgies, D.-M.; Toombes, G. E. S.; Hillmyer, M. A.; Ludwigs, S.; Steiner, U.; *et al.* A Bicontinuous Double Gyroid Hybrid Solar Cell. *Nano Lett.* **2009**, *9*, 2807–2812.
38. Docampo, P.; Stefik, M.; Guldin, S.; Gunning, R.; Yufa, N. A.; Cai, N.; Wang, P.; Steiner, U.; Wiesner, U.; Snaith, H. J. Triblock-Terpolymer-Directed Self-Assembly of Mesoporous TiO_2: High-Performance Photoanodes for Solid-State Dye-Sensitized Solar Cells. *Adv. Energy Mater.* **2012**, *2*, 676–682.
39. Polman, A.; Atwater, H. A. Photonic Design Principles for Ultrahigh-Efficiency Photovoltaics. *Nat. Mater.* **2012**, *11*, 174–177.
40. Lunt, R. R.; Osedach, T. P.; Brown, P. R.; Rowehl, J. A.; Bulović, V. Practical Roadmap and Limits to Nanostructured Photovoltaics. *Adv. Mater.* **2011**, *23*, 5712–5727.
41. Orilall, M. C.; Wiesner, U. Block Copolymer Based Composition and Morphology Control in Nanostructured Hybrid Materials for Energy Conversion and Storage: Solar Cells, Batteries, and Fuel Cells. *Chem. Soc. Rev.* **2011**, *40*, 520–535.
42. Templin, M.; Franck, A.; Chesne, A. D.; Leist, H.; Zhang, Y.; Ulrich, R.; Schädler, V.; Wiesner, U. Organically Modified Aluminosilicate Mesostructures from Block Copolymer Phases. *Science* **1997**, *278*, 1795–1798.
43. Guo, C.; Lin, Y.-H.; Witman, M. D.; Smith, K. A.; Wang, C.; Hexemer, A.; Strzalka, J.; Gomez, E. D.; Verduzco, R. Conjugated Block Copolymer Photovoltaics with near 3% Efficiency through Microphase Separation. *Nano Lett.* **2013**, *13*, 2957–2963.
44. Kuemmel, M.; Grosso, D.; Boissière, C.; Smarsly, B.; Brezesinski, T.; Albouy, P. A.; Amenitsch, H.; Sanchez, C. Thermally Stable Nanocrystalline γ-Alumina Layers with Highly Ordered 3D Mesoporosity. *Angew. Chem., Int. Ed.* **2005**, *44*, 4589–4592.
45. Oveisi, H.; Jiang, X.; Imura, M.; Nemoto, Y.; Sakamoto, Y.; Yamauchi, Y. A Mesoporous γ-Alumina Film with Vertical Mesoporosity: The Unusual Conversion from a $Im\bar{3}m$ Mesostructure to Vertically Oriented γ-Alumina Nanowires. *Angew. Chem., Int. Ed.* **2011**, *50*, 7410–7413.
46. Jiang, X.; Suzuki, N.; Bastakoti, B. P.; Wu, K. C.-W.; Yamauchi, Y. Synthesis of Continuous Mesoporous Alumina Films with Large-Sized Cage-Type Mesopores by Using Diblock Copolymers. *Chem.—Asian J.* **2012**, *7*, 1713–1718.
47. Guldin, S.; Kolle, M.; Stefik, M.; Langford, R.; Eder, D.; Wiesner, U.; Steiner, U. Tunable Mesoporous Bragg Reflectors Based on Block-Copolymer Self-Assembly. *Adv. Mater.* **2011**, *23*, 3664–3668.
48. Rauda, I. E.; Buonsanti, R.; Saldarriaga-Lopez, L. C.; Benjauthrit, K.; Schelhas, L. T.; Stefik, M.; Augustyn, V.; Ko, J.; Dunn, B.; Wiesner, U.; *et al.* General Method for the Synthesis of Hierarchical Nanocrystal-Based Mesoporous Materials. *ACS Nano* **2012**, *6*, 6386–6399.
49. Buonsanti, R.; Pick, T. E.; Krins, N.; Richardson, T. J.; Helms, B. A.; Milliron, D. J. Assembly of Ligand-Stripped Nanocrystals into Precisely Controlled Mesoporous Architectures. *Nano Lett.* **2012**, *12*, 3872–3877.
50. Nedelcu, M.; Lee, J.; Crossland, E. J. W.; Warren, S. C.; Orilall, M. C.; Guldin, S.; Hüttner, S.; Ducati, C.; Eder, D.; Wiesner, U.; *et al.* Block Copolymer Directed Synthesis of Mesoporous TiO_2 for Dye-Sensitized Solar Cells. *Soft Matter* **2009**, *5*, 134–139.
51. Arora, H.; Du, P.; Tan, K. W.; Hyun, J. K.; Grazul, J.; Xin, H. L.; Muller, D. A.; Thompson, M. O.; Wiesner, U. Block Copolymer Self-Assembly-Directed Single-Crystal Homo- and Heteroepitaxial Nanostructures. *Science* **2010**, *330*, 214–219.

52. Guldin, S.; Hüttner, S.; Tiwana, P.; Orilall, M. C.; Ulgüt, B.; Stefik, M.; Docampo, P.; Kolle, M.; Divitini, G.; Ducati, C.; *et al.* Improved Conductivity in Dye-Sensitised Solar Cells through Block-Copolymer Confined TiO_2 Crystallisation. *Energy Environ. Sci.* **2010**, *4*, 225–233.
53. Hur, K.; Francescato, Y.; Giannini, V.; Maier, S. A.; Hennig, R. G.; Wiesner, U. Three-Dimensionally Isotropic Negative Refractive Index Materials from Block Copolymer Self-Assembled Chiral Gyroid Networks. *Angew. Chem., Int. Ed.* **2011**, *50*, 11985–11989.
54. Baikie, T.; Fang, Y.; Kadro, J. M.; Schreyer, M.; Wei, F.; Mhaisalkar, S. G.; Graetzel, M.; White, T. J. Synthesis and Crystal Chemistry of the Hybrid Perovskite $(CH_3NH_3)PbI_3$ for Solid-State Sensitised Solar Cell Applications. *J. Mater. Chem. A* **2013**, *1*, 5628–5641.
55. Poglitsch, A.; Weber, D. Dynamic Disorder in Methylammoniumtrihalogenoplumbates (II) Observed by Millimeter-Wave Spectroscopy. *J. Chem. Phys.* **1987**, *87*, 6373–6378.
56. Stoumpos, C. C.; Malliakas, C. D.; Kanatzidis, M. G. Semiconducting Tin and Lead Iodide Perovskites with Organic Cations: Phase Transitions, High Mobilities, and Near-Infrared Photoluminescent Properties. *Inorg. Chem.* **2013**, *52*, 9019–9038.
57. Busch, P.; Rauscher, M.; Smilgies, D.-M.; Posselt, D.; Papadakis, C. M. Grazing-Incidence Small-Angle X-Ray Scattering from Thin Polymer Films with Lamellar Structures—The Scattering Cross Section in the Distorted-Wave Born Approximation. *J. Appl. Crystallogr.* **2006**, *39*, 433–442.
58. Bian, K.; Choi, J. J.; Kaushik, A.; Clancy, P.; Smilgies, D.-M.; Hanrath, T. Shape-Anisotropy Driven Symmetry Transformations in Nanocrystal Superlattice Polymorphs. *ACS Nano* **2011**, *5*, 2815–2823.
59. D. Yoreo, J.; Vekilov, P. G. Principles of Crystal Nucleation and Growth. In *Biomineralization*; Dove, P. M., De Yoreo, J., Weiner, S., Eds.; Mineralogical Society of America: Washington, D.C., 2003; Vol. 54, pp 57−93.
60. Vekilov, P. G. Nucleation. *Cryst. Growth Des.* **2010**, *10*, 5007–5019.
61. Smilgies, D.-M.; Blasini, D. R. Indexation Scheme for Oriented Molecular Thin Films Studied with Grazing-Incidence Reciprocal-Space Mapping. *J. Appl. Crystallogr.* **2007**, *40*, 716–718.
62. Hammersley, A. P.; Svensson, S. O.; Hanfland, M.; Fitch, A. N.; Hausermann, D. Two-Dimensional Detector Software: From Real Detector to Idealised Image or Two-Theta Scan. *High Pressure Res.* **1996**, *14*, 235–248.